

Article

Doping Engineering for Optimizing Piezoelectric and Elastic Performance of AlN

Xi Yu ^{1,†}, Lei Zhu ^{2,†}, Xin Li ³, Jia Zhao ², Tingjun Wu ², Wenjie Yu ^{2,3} and Weimin Li ^{1,2,3,*}

¹ School of Microelectronics, Shanghai University, Shanghai 201899, China

² State Key Laboratory of Functional Materials for Informatics, Shanghai Institute of Microsystem and Information Technology, Chinese Academy of Sciences, Shanghai 200050, China

³ Shanghai Institute of IC Materials Co., Ltd., Shanghai 201899, China

* Correspondence: weimin.li@mail.sim.ac.cn

† These authors contributed equally to this work.

Abstract: The piezoelectric and elastic properties are critical for the performance of AlN-based 5G RF filters. The improvement of the piezoelectric response in AlN is often accompanied by lattice softening, which compromises the elastic modulus and sound velocities. Optimizing both the piezoelectric and elastic properties simultaneously is both challenging and practically desirable. In this work, 117 $X_{0.125}Y_{0.125}Al_{0.75}N$ compounds were studied with the high-throughput first-principles calculation. $B_{0.125}Er_{0.125}Al_{0.75}N$, $Mg_{0.125}Ti_{0.125}Al_{0.75}N$, and $Be_{0.125}Ce_{0.125}Al_{0.75}N$ were found to have both high C_{33} (>249.592 GPa) and high e_{33} (>1.869 C/m²). The COMSOL Multiphysics simulation showed that most of the quality factor (Q_r) values and the effective coupling coefficient (k_{eff}^2) of the resonators made with these three materials were higher than those with $Sc_{0.25}AlN$ with the exception of the k_{eff}^2 of $Be_{0.125}Ce_{0.125}AlN$, which was lower due to the higher permittivity. This result demonstrates that double-element doping of AlN is an effective strategy to enhance the piezoelectric strain constant without softening the lattice. A large e_{33} can be achieved with doping elements having d-/f- electrons and large internal atomic coordinate changes of $du/d\varepsilon$. The doping elements–nitrogen bond with a smaller electronegativity difference (ΔEd) leads to a larger elastic constant C_{33} .

Keywords: first-principles calculation; high-throughput; aluminum nitride; piezoelectric coefficient; elastic modulus

Citation: Yu, X.; Zhu, L.; Li, X.;

Zhao, J.; Wu, T.; Yu, W.; Li, W.

Doping Engineering for Optimizing Piezoelectric and Elastic

Performance of AlN. *Materials* **2023**,

16, 1778.

<https://doi.org/10.3390/ma16051778>

Academic Editors: Aleksander Czekanski and Cuiying Jian

Received: 21 November 2022

Revised: 22 December 2022

Accepted: 27 December 2022

Published: 21 February 2023



Copyright: © 2023 by the authors. Licensee MDPI, Basel, Switzerland. This article is an open access article distributed under the terms and conditions of the Creative Commons Attribution (CC BY) license (<https://creativecommons.org/licenses/by/4.0/>).

1. Introduction

Piezoelectric materials, which can be applied to Radio Frequency (RF) filters, have drawn much attention with the commercialization of 5G communication technologies [1–4]. Aluminum nitride with wurtzite structure (w-AlN) is the prevailing piezoelectric material for the body acoustic wave (BAW) filters owing to the advantages of high acoustic velocity, minimal acoustic loss, high thermal stability, and good compatibility with Complementary Metal Oxide Semiconductor (CMOS) technology [5,6]. The critical parameters to evaluate the performance of piezoelectric materials for 5G filters are the mechanical quality factor (Q) and the longitudinal electromechanical coupling constant (k_{33}^2). The higher the Q , the lower the mechanical loss. The higher the k_{33}^2 , the larger the frequency bandwidth. In general, the Q value of 5G RF filters based on w-AlN thin film ($Q = 400$) is higher than that based on ZnO thin film ($Q = 350$), achieving low acoustic loss [7]. However, the k_{33}^2 (6.1%) [8] of undoped w-AlN is lower than some well-known piezoelectric materials, such as lead zirconate titanate perovskite (PZT) ($k_{33}^2 = 8–15\%$) [8] and ZnO ($k_{33}^2 = 7.5\%$) [8]; therefore, undoped w-AlN needs further optimization [9].

As shown in Equations (1) and (2), the characteristic Q and k_{33}^2 of a BAW RF filter are affected by the piezoelectric strain constant (e_{33}) and elastic constant (C_{33}) of the piezoelectric material [10–12],

$$\frac{1}{k_{33}^2} = \frac{C_{33}\epsilon_{33}^s}{e_{33}^2} + 1, \quad (1)$$

$$Q = \frac{C_{33} + e_{33}^2/\epsilon_{33}^s}{\omega\eta_{33}}, \quad (2)$$

where Q , ϵ_{33}^s , ω , and η_{33} are the acoustic quality factor, the clamped permittivity, the angular frequency, and the viscosity coefficient (details are shown in the support information) along the c -axis direction, respectively. A high C_{33} is favorable to Q , and a high e_{33} is favorable to k_{33}^2 . The piezoelectric material coupling coefficient k_{33}^2 and resonator effective coupling coefficient K_{eff}^2 are positively related. It is not hard to design a resonator with a high K_{eff}^2 from a material having a high k_{33}^2 value [13]. Consequently, w -AlN should be tailored to have a high C_{33} and e_{33} , simultaneously, which has been proven to be a difficult task.

For example, first-principles calculations [14] and experiments [15] showed that an ~400% increase in the piezoelectric coefficient ($d_{33} \approx e_{33}/C_{33}$) of w -AlN can be achieved with Sc doping. The increase in the e_{33} is caused by the increase in the sensitivity of the internal atomic coordinates in response to the strain ($du/d\epsilon$) [16]. However, there also exists an elastic softening, owing to the elongated energy landscape in the c/a direction [17]. The e_{33} of w - $X_{a/2}Y_{a/2}Al_{1-a}N$ ($X = Li$; $Y = V, Nb, Ta$; $a = 0.125, 0.25, 0.375$) is enhanced compared to that of undoped w -AlN [18], while the C_{33} decreases simultaneously due to the fact that these dopants can lead to a phase transition to a non-polar hexagonal structure. Hirata et al. [19] used first-principles calculations to investigate the enhancement in piezoelectric properties and the reduction in elastic properties by co-doping w - $X_{a/2}Y_{a/2}Al_{1-a}N$ ($X = Mg$; $Y = Nb, Ti, Zr, Hf$; $a = 0.125$). The bonding analysis of the metal–nitrogen pairs by co-doping $Mg + Y$ into w -AlN was carried out by the crystal orbital Hamilton population (COHP), which showed that weaker bonding energy is one of the reasons for the elastic softening.

The above results showed the need for a new mechanism to achieve a high C_{33} and e_{33} simultaneously. Manna et al. [20] found that the co-doping of Y and B elements in w -AlN improved the elastic properties while retaining good piezoelectric performance. Subsequently, Jing et al. [21] discovered that the C_{33} of $B_{0.125}Sc_{x-0.125}Al_{1-x}N$ is higher than that of $Sc_xAl_{1-x}N$ with a small enhancement of the e_{33} . These results confirm the feasibility of improving the piezoelectric and elastic properties by dual-element co-doping [22,23]. However, there is still a lack of systematic analysis leading to a clear strategy to choose doping elements for the enhancement of both the C_{33} and e_{33} . Therefore, expanding the map of doping elements and the understanding of the adjustment mechanism is critical to finding new doping schemes with excellent performance.

In this work, a high-throughput workflow is designed to calculate the piezoelectricity and elasticity of 117 $X_{0.125}Y_{0.125}Al_{0.75}N$ compounds. Filtered by the non-magnetic criteria, semiconductor criteria, stability criteria, and performance criteria, three dopants are finally screened out, which are $B_{0.125}Er_{0.125}Al_{0.75}N$ ($e_{33} = 2.11$ C/m², $C_{33} = 262.2$ GPa, $d_{33} = 8.05$ pC/N), $Mg_{0.125}Ti_{0.125}Al_{0.75}N$ ($e_{33} = 2.41$ C/m², $C_{33} = 261.1$ GPa, $d_{33} = 9.22$ pC/N), and $Be_{0.125}Ce_{0.125}Al_{0.75}N$ ($e_{33} = 2.12$ C/m², $C_{33} = 272.0$ GPa, $d_{33} = 7.78$ pC/N). All have higher piezoelectric and elastic properties than $Sc_{0.25}Al_{0.75}N$ ($e_{33} = 1.87$ C/m², $C_{33} = 249.59$ GPa, $d_{33} = 7.49$ pC/N). It is found that the primary factor influencing the C_{33} is the electronegativity difference (ΔEd) of the metal–nitrogen bonds, and the primary factor influencing the e_{33} is the $du/d\epsilon$ of the doping atoms. The bonds with a small ΔEd in the doped-AlN between the doping elements and nitrogen with stronger strength leads to a larger elastic constant C_{33} . The energy competition between the doping atoms and Al mainly affects the internal structural response ($du/d\epsilon$) of the crystal due to the transition elements doping into tetrahedral Al sites, tending to form non-tetrahedral coordinates, and undergoing excursions. The increasing of C_{33} from the electronegativity difference and e_{33} from the $du/d\epsilon$ of the

doping atom with d-/f- electrons provides clear ideas to design new piezoelectric materials for 5G filters.

2. Computational Details

The $2 \times 2 \times 2$ supercells for $w\text{-X}_{0.125}\text{Y}_{0.125}\text{Al}_{0.75}\text{N}$ (Figure 1b) were built with the special quasi-random structures (SQS) method [24]. The first-principles calculations were performed with the Vienna Ab initio Simulation Package (VASP) [25–27]. The Perdew–Burke–Ernzerhof (PBE) type generalized gradient approximation (GGA) as the exchange–correlation function was implemented [24]. The elastic tensor was determined by performing the finite differences method. Six finite distortions of the lattice were taken, and the corresponding elastic constants could be derived from the strain–stress relationship [28]. The strains for the original structure along each of the Cartesian directions were $\pm 0.5\%$ and $\pm 1\%$. The piezoelectric tensors were evaluated from the phonon and dielectric response calculations performed from the density functional perturbation theory (DFPT) [29–31]. The Monkhorst–Pack method [32] was used to set the k-point mesh. The k-grids used in the calculation of the structural optimization, self-consistent, and C_{ij}/e_{ij} were $30/L+1$, $60/L+1$, and $30/L+1$, respectively, where L is the lattice constant of the systems. The cutoff energy of all calculations was 520 eV. The convergence criteria for the energy and force were set to 10^{-4} eV and 10^{-2} eV/Å, respectively. The Hubbard U values were from Wang et al. and Dudarev et al. [33,34].

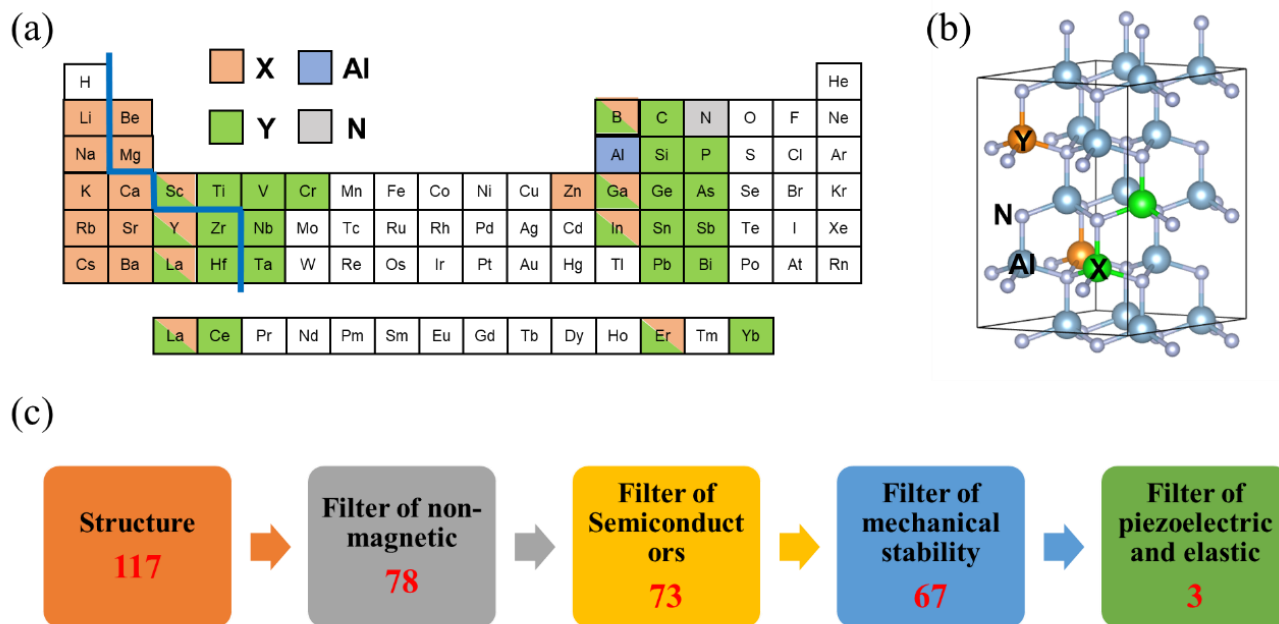


Figure 1. High-throughput workflow of screening piezoelectric material $w\text{-X}_{0.125}\text{Y}_{0.125}\text{Al}_{0.75}\text{N}$. (a) Dopants considered in this study. The blue line separates elements X and Y according to an ΔEd less than/more than 1.7. (b) Crystal structure of $w\text{-X}_{0.125}\text{Y}_{0.125}\text{Al}_{0.75}\text{N}$. (c) High-throughput workflow of screening $\text{X}_{0.125}\text{Y}_{0.125}\text{Al}_{0.75}\text{N}$ with a high e_{33} and high C_{33} . The red numbers indicate the number of remaining systems after screening.

The two-dimensional sandwich structure of the resonator and its geometric parameters is shown in Figure S1. The resonator consists of a piezoelectric material with top and bottom electrodes. COMSOL Multiphysics 6.0 is used to simulate the resonator quality factor (Q_r) and effective electromechanical coupling coefficient (k_{eff}^2) of the resonator by using the finite element method [35]. Among them, the 2nd order Taylor approximation

was performed to simulate the k_{eff}^2 [36]. The Q_r value was calculated using the method proposed by Bode et al. [37]. The physical parameters of the materials utilized in the simulation are shown in Table S1.

3. Results

To explore the theoretical feasibility of doping engineering to obtain materials with a high performance of large e_{33} and C_{33} , 117 dopants of $X_{0.125}Y_{0.125}Al_{0.75}N$ without toxic elements were tested. As shown in Figure 1a, the orange, green, blue, and gray spheres indicate X, Y, Al, and N, respectively. Considering the charge conservation law, the reasonable elements X and Y are substituted to the Al sites by 1:1. Moreover, Sc, Y, La Er, B, Ga, and In elements can be doped into either the X site or Y site due to the valence of +3. To effectively screen the piezoelectric and elastic performance of $X_{0.125}Y_{0.125}Al_{0.75}N$ materials, a high-throughput workflow was designed (Figure 1c). First, the entries with complex magnetism were removed due to the difficulties to accurately calculate the properties of the magnetic materials for the high-throughput method. Second, the non-semiconductor systems were removed. If the band gap of $X_{0.125}Y_{0.125}Al_{0.75}N$ is less than 0, it indicates that the system is metallic and is not suitable for making piezoelectric layers for 5G filters. Then, the mechanical criterion was tested by the Born–Huang criteria of hexagonal structures [38]: $C_{11} > C_{12}$, $2C_{13}^2 < C_{33}(C_{11} + C_{12})$, $C_{44} > 0$, $C_{66} > 0$. It is clear that all of the models we considered were mechanically stable, and the detailed results are listed in Table S2. Finally, three dopants ($B_{0.125}Er_{0.125}Al_{0.75}N$, $Mg_{0.125}Ti_{0.125}Al_{0.75}N$, and $Be_{0.125}Ce_{0.125}Al_{0.75}N$) were screened out as having better performance than $Sc_{0.25}Al_{0.75}N$. For comparison purposes, the calculation results of $Sc_{0.25}Al_{0.75}N$ were $e_{33} = 1.87$ C/m², $C_{33} = 249.59$ GPa, and $d_{33} = 7.49$ pC/N, consistent with the results reported by Caro et al., Tasnadi et al., etc. [14,15,39–41]. (Details can be found in Figure S2).

The detailed results of the 67 mechanically stable dopants are shown in Table 1. The modulation ranges of the e_{33} and C_{33} are 0.064–2.408 C/m² and 165.556–396.671 GPa, respectively. Table 1 shows that the e_{33} of the dopants with small atomic radii elements and transition elements is high. The e_{33} of the dopants with large atomic radii, such as K, Rb, Ca, Sr, Ba, and La, is smaller than that of those with small atomic radii, such as Li and Mg. Furthermore, the dopants that have one small radii element and one transition element (e.g., Mg co-doped with Ce, Ti, Hf, and Zr) show a higher e_{33} than Mg co-doping with carbon group elements (i.e., C, Si, Ge, Sn, and Pb). For the C_{33} , when the difference between the electronegativity of the doping atom and the N element is small, the C_{33} is always high. For example, $Be_{0.125}Ce_{0.125}Al_{0.75}N$ has an $\Delta Ed = 0.98$ and a $C_{33} = 346.605$ GPa. Comprehensively considering the e_{33} and C_{33} , $B_{0.125}Er_{0.125}Al_{0.75}N$, $Mg_{0.125}Ti_{0.125}Al_{0.75}N$, and $Be_{0.125}Ce_{0.125}Al_{0.75}N$, all having non-transition elements and a small atomic radii atom with a small ΔEd and transition elements co-doping, have good performance. It is worth noting that $Li_{0.125}Ta_{0.125}Al_{0.75}N$, $Mg_{0.125}Hf_{0.125}Al_{0.75}N$, and $Mg_{0.125}Zr_{0.125}Al_{0.75}N$, which have a C_{33} only somewhat smaller than $Sc_{0.25}Al_{0.75}N$ and both an e_{33} and a d_{33} larger than $Sc_{0.25}Al_{0.75}N$, are also excellent choices. Better performance can be expected if the doping concentration is further regulated.

Table 1. Properties of the e_{33} , C_{33} , d_{33} , and band gap of the 67 dopants considered in this study.

Group	Chemical Formula	C_{33} (GPa)	e_{33} (C/m ²)	d_{33} (pC/N)	Band Gap (eV)
IA(X) + VA/VB(Y)	$Li_{0.125}As_{0.125}Al_{0.75}N$	294.397	1.539	5.227	1.026
	$Li_{0.125}Nb_{0.125}Al_{0.75}N$	224.598	2.221	9.890	1.809
	$Li_{0.125}Sb_{0.125}Al_{0.75}N$	183.151	0.155	0.849	1.234
	$Li_{0.125}Ta_{0.125}Al_{0.75}N$	245.201	2.242	9.143	2.177
	$Na_{0.125}Ta_{0.125}Al_{0.75}N$	177.679	1.740	9.793	1.950
	$K_{0.125}Nb_{0.125}Al_{0.75}N$	258.451	0.961	3.717	1.308
	$K_{0.125}Ta_{0.125}Al_{0.75}N$	213.903	0.064	0.301	1.704
	$Rb_{0.125}Ta_{0.125}Al_{0.75}N$	222.589	0.704	3.165	1.095

	Rb _{0.125} V _{0.125} Al _{0.75} N	249.936	1.037	4.151	1.011
	Be _{0.125} C _{0.125} Al _{0.75} N	346.605	1.749	4.627	1.808
	Be _{0.125} Ce _{0.125} Al _{0.75} N	271.992	2.115	7.776	1.434
	Be _{0.125} Ge _{0.125} Al _{0.75} N	350.546	1.195	3.408	3.149
	Be _{0.125} Hf _{0.125} Al _{0.75} N	288.143	1.985	6.888	3.504
	Be _{0.125} Pb _{0.125} Al _{0.75} N	326.451	1.224	3.748	1.573
	Be _{0.125} Si _{0.125} Al _{0.75} N	356.115	1.176	3.303	3.959
	Be _{0.125} Sn _{0.125} Al _{0.75} N	328.447	1.508	4.591	2.490
	Be _{0.125} Ti _{0.125} Al _{0.75} N	294.069	2.042	6.945	3.098
	Be _{0.125} Zr _{0.125} Al _{0.75} N	274.419	2.042	7.440	3.471
	Mg _{0.125} C _{0.125} Al _{0.75} N	317.855	1.641	5.164	2.604
	Mg _{0.125} Ce _{0.125} Al _{0.75} N	247.040	1.808	7.317	1.050
	Mg _{0.125} Ge _{0.125} Al _{0.75} N	314.839	1.492	4.740	2.355
	Mg _{0.125} Hf _{0.125} Al _{0.75} N	245.935	2.215	9.008	3.124
	Mg _{0.125} Pb _{0.125} Al _{0.75} N	294.874	1.544	5.238	1.025
	Mg _{0.125} Si _{0.125} Al _{0.75} N	321.218	1.632	5.081	2.891
	Mg _{0.125} Sn _{0.125} Al _{0.75} N	304.080	1.545	5.080	2.273
	Mg _{0.125} Ti _{0.125} Al _{0.75} N	261.105	2.408	9.223	2.744
	Mg _{0.125} Zr _{0.125} Al _{0.75} N	243.235	2.180	8.962	2.947
IIA(X) + IVA/IVB(Y)	Ca _{0.125} Ce _{0.125} Al _{0.75} N	253.372	1.484	5.858	1.282
	Ca _{0.125} Ge _{0.125} Al _{0.75} N	258.318	1.549	5.995	1.677
	Ca _{0.125} Hf _{0.125} Al _{0.75} N	260.880	1.660	6.363	2.644
	Ca _{0.125} Pb _{0.125} Al _{0.75} N	252.145	1.440	5.712	0.532
	Ca _{0.125} Si _{0.125} Al _{0.75} N	291.283	1.595	5.477	2.523
	Ca _{0.125} Sn _{0.125} Al _{0.75} N	256.727	1.628	6.340	1.549
	Ca _{0.125} Ti _{0.125} Al _{0.75} N	259.020	1.841	7.107	2.370
	Ca _{0.125} Zr _{0.125} Al _{0.75} N	219.511	1.899	8.650	2.425
	Sr _{0.125} Ge _{0.125} Al _{0.75} N	239.683	0.161	0.672	1.509
	Sr _{0.125} Hf _{0.125} Al _{0.75} N	182.913	0.595	3.251	1.400
	Sr _{0.125} Si _{0.125} Al _{0.75} N	276.980	0.466	1.682	2.327
	Sr _{0.125} Sn _{0.125} Al _{0.75} N	257.722	0.950	3.687	1.620
	Sr _{0.125} Ti _{0.125} Al _{0.75} N	202.510	1.440	7.112	1.597
	Sr _{0.125} Zr _{0.125} Al _{0.75} N	265.455	1.358	5.114	1.824
	Ba _{0.125} C _{0.125} Al _{0.75} N	173.168	1.280	7.393	1.644
	Ba _{0.125} Ce _{0.125} Al _{0.75} N	240.387	0.850	3.538	0.973
	Ba _{0.125} Hf _{0.125} Al _{0.75} N	217.607	0.836	3.841	1.757
	Ba _{0.125} Si _{0.125} Al _{0.75} N	278.275	0.444	1.596	1.423
	Ba _{0.125} Sn _{0.125} Al _{0.75} N	309.324	0.520	1.682	0.382
	Ba _{0.125} Ti _{0.125} Al _{0.75} N	227.211	1.289	5.672	1.582
	Ba _{0.125} Zr _{0.125} Al _{0.75} N	165.556	0.745	4.497	0.929
IIIA/IIIB(X) + IIIA/IIIB(Y)	B _{0.125} Er _{0.125} Al _{0.75} N	262.248	2.112	8.052	2.883
	B _{0.125} Ga _{0.125} Al _{0.75} N	396.671	1.202	3.030	3.533
	B _{0.125} La _{0.125} Al _{0.75} N	253.881	0.683	2.690	1.918
	B _{0.125} Sc _{0.125} Al _{0.75} N	309.808	1.888	6.093	3.005
	B _{0.125} Y _{0.125} Al _{0.75} N	284.759	2.045	7.180	2.659
	Sc _{0.125} Ga _{0.125} Al _{0.75} N	300.226	1.543	5.141	3.532
	Sc _{0.125} La _{0.125} Al _{0.75} N	249.583	1.440	5.769	2.098
	Sc _{0.125} Y _{0.125} Al _{0.75} N	222.807	2.026	9.092	2.729
	Er _{0.125} Ga _{0.125} Al _{0.75} N	293.187	1.359	4.634	2.848
	Er _{0.125} La _{0.125} Al _{0.75} N	273.622	1.229	4.490	1.972
	Er _{0.125} Sc _{0.125} Al _{0.75} N	225.194	1.877	8.337	2.788

Er _{0.125} Y _{0.125} Al _{0.75} N	231.736	1.706	7.362	2.339
In _{0.125} B _{0.125} Al _{0.75} N	349.798	1.342	3.837	2.462
In _{0.125} Ga _{0.125} Al _{0.75} N	348.935	1.260	3.611	2.844
In _{0.125} Sc _{0.125} Al _{0.75} N	281.114	1.624	5.778	2.898
In _{0.125} Y _{0.125} Al _{0.75} N	271.097	1.404	5.180	2.318
La _{0.125} Ga _{0.125} Al _{0.75} N	270.619	1.368	5.056	2.001
Y _{0.125} Ga _{0.125} Al _{0.75} N	306.706	1.418	4.623	2.886
Y _{0.125} La _{0.125} Al _{0.75} N	265.515	1.407	5.298	1.950
w-AlN	359.862	1.471	4.087	4.056
Sc _{0.25} Al _{0.75} N	249.592	1.869	7.488	3.287

4. Discussion

4.1. Analysis of Elastic Properties

As shown in Figure 2, we explored in detail the mechanism of co-doping to enhance the characteristics of the C_{33} and e_{33} , respectively. The hardness of the crystal is positively related to the bond density and negatively related to the ionicity indicator f_i [42–44]. Figure 2a is the relationship of the C_{33} and the electronegativity difference ΔEd ,

$$\Delta Ed = \frac{(E_X + E_Y - 2E_N)}{2}, \quad (3)$$

where E_X , E_Y , and E_N are the electronegativity of elements X, Y, and N, respectively. The electronegativity difference indicates the ionicity indicator (f_i) of the chemical bonds according to the Pauling for AB-type compounds [45],

$$f_i\% = (1 - e^{-\frac{1}{4}(\Delta Ed)^2}) \times 100, \quad (4)$$

where f_i indicates the degree of ionization of the hybrid bonds with a larger f_i indicating that the chemical bond is closer to an ionic bond. Figure 2a shows that the C_{33} is negatively related to the ΔEd (i.e., the smaller the difference of electronegativity, the smaller the f_i and the larger the C_{33}). Moreover, other factors, such as the bond density induced by lattice distortion, also slightly influence the C_{33} . A specific mechanistic explanation of the effect of lattice distortion on the C_{33} can be found in the supporting information. Generally, the smaller the electronegativity difference, the smaller the degree of ionization of the metal-N in $X_{0.125}Y_{0.125}Al_{0.75}N$ and the larger the hardness of the crystal. Thus, the electronegativity difference could be a criterion for the selected doped-AlN with a high C_{33} .

4.2. Analysis of Piezoelectric Properties

Figure 2b shows the distribution of the e_{33} , which comprises an electronic-response part and ion-polarization part [46].

$$e_{33} = e_{33}^{clamped} + e_{33}^{non_clamped} \quad (5)$$

$e_{33}^{clamped}$ represents the electronic response under strain, which is evaluated by fixing the internal atomic coordinates at their equilibrium positions. $e_{33}^{non_clamped}$ represents the ion polarization under strain, which is derived from the internal atomic coordinate changes. The mean and standard deviation of the $e_{33}^{non_clamped}$ are 2.001 and 0.689, respectively. However, the mean and standard deviation of the $e_{33}^{clamped}$ are −0.435 and 0.077, respectively. Obviously, the $e_{33}^{non_clamped}$ mainly contributes the e_{33} of w-AlN, owing to wider adjustable values and larger weights. Here, we focus on the derivation of the ion-polarization part,

$$e_{33}^{non_clamped} = \sum_n \frac{2eZ_{33}(n)}{\sqrt{3}a^2} \frac{du(n)}{d\epsilon}, \quad (6)$$

where n runs on all atoms in the supercell, e is the elementary charge, and a is the equilibrium lattice constant. Z_{33} is the c -axis component of the dynamic Born charge tensor, and $du/d\epsilon$ is the strain sensitivity. u is the ratio of the length of the metal-N along the c -axis

(uc) to the lattice constant c in w-AlN (Figure 2c), which can be changed by the strain in the c direction. $du/d\varepsilon$ is the factor about the c -structure change, and Z_{33} is the factor about the piezoelectric polarization variation on the structure change. Based on the first-principles calculation, the average Z_{33} is 2.77 and can be adjusted from -6.48% to 8.53% ; the average $du/d\varepsilon$ is 0.17 and can be adjusted from -90.89% to 27.10% . The variation of the $du/d\varepsilon$ is particularly large, which may significantly affect the $e_{33}^{non_clamped}$ [16,47].

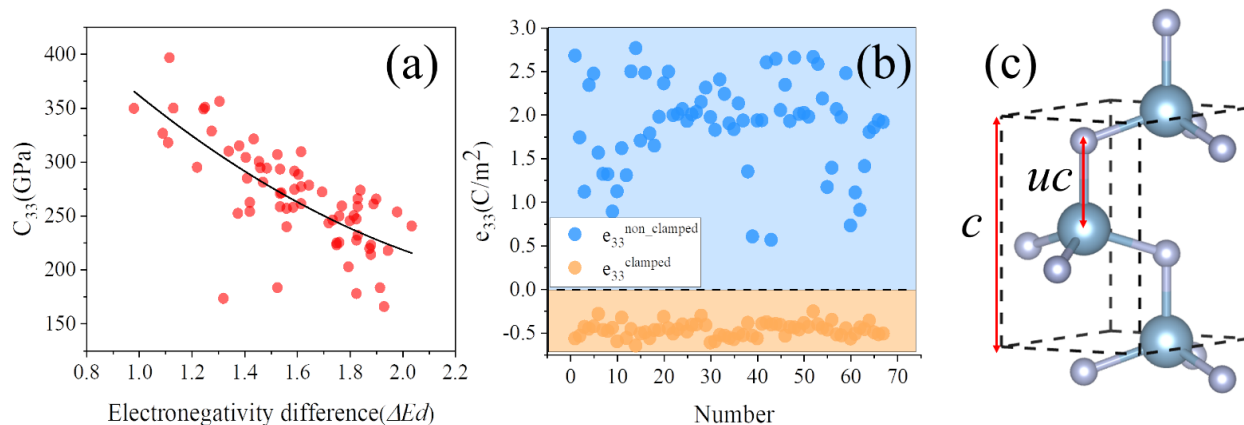


Figure 2. (a) The relationship of the C_{33} and electronegativity difference. The result of the quadratic fitting is shown as a solid line. (b) The $e_{33}^{non_clamped}$ and $e_{33}^{clamped}$ of $X_{0.125}Y_{0.125}Al_{0.75}N$. (c) Wurtzite structure with the internal parameter $u = uc/c$.

Figure 3a shows that there is a linear correlation between the $du/d\varepsilon$ along the c -axis and the e_{33} . The $du/d\varepsilon$ of w-AlN is calculated by varying the doping atoms with an adjustment of the internal structure parameter, especially the structure parameter along the c -axis. For example, $Mg_{0.125}Ti_{0.125}Al_{0.75}N$, $Li_{0.125}Ta_{0.125}Al_{0.75}N$, and $B_{0.125}Er_{0.125}Al_{0.75}N$ have large distortions along the c -axis with a $du/d\varepsilon = 0.221$, 0.224 , and 0.225 , respectively, and an e_{33} reaching 2.41 , 2.24 , and 2.11 C/m², respectively. In contrast, $Mg_{0.125}Ge_{0.125}Al_{0.75}N$, $Li_{0.125}Sb_{0.125}Al_{0.75}N$, and $B_{0.125}Ga_{0.125}Al_{0.75}N$ have a small distortion along the c -axis with a $du/d\varepsilon$ of 0.178 , 0.0152 , 0.152 , respectively, and an e_{33} of only 1.492 , 0.155 , and 1.202 C/m², respectively. Figure 3b shows that the variation range of $|du/d\varepsilon|$ of the doping elements X and Y is much larger than that of Al and N. The average $|du/d\varepsilon|$ of the doping elements X and Y is 0.195 and 0.184 , respectively, while that of the elements Al and N is only 0.0597 and 0.0836 , respectively. Thus, the doping elements affect the e_{33} dominantly compared to Al and N. The systems with large lattice distortion are doped by Sc, Y, and other transition elements with d-electrons and f-electrons.

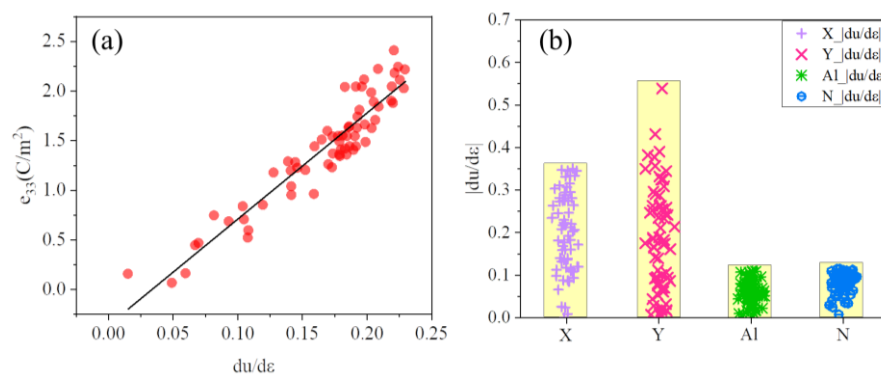


Figure 3. (a) The relationship of the e_{33} and $du/d\varepsilon$. $du/d\varepsilon$ is measured by calculating the response of the $u(n)$ under a macroscopic strain ($\eta = 0.5\%$). The result of the linear fitting is shown as a solid line. (b) The $|du/d\varepsilon|$ of X, Y, Al, and N in $X_{0.125}Y_{0.125}Al_{0.75}N$ alloys.

To further discuss the mechanism of transition elements affecting the lattice distortion, the band structures and wave functions of the $\text{Mg}_{0.125}\text{Ti}_{0.125}\text{Al}_{0.75}\text{N}$ and $\text{Mg}_{0.125}\text{Ge}_{0.125}\text{Al}_{0.75}\text{N}$ system were calculated. The doping atoms replace the Al sites, thus the valence band of the undoped and doped w-AlN are all the p-electrons of the N atom. The doping atoms mainly change the electronic state of the conduction band. As shown in Figure 4a,b, the conduction bands of $\text{Mg}_{0.125}\text{Ti}_{0.125}\text{Al}_{0.75}\text{N}$ and $\text{Mg}_{0.125}\text{Ge}_{0.125}\text{Al}_{0.75}\text{N}$ are occupied by the d-electrons of Ti and s-electrons of Ge, respectively. The sp^3 hybridization of w-AlN leads to a tetrahedral coordination geometry of Al; in addition, the doping atoms only have s- and p- electron orbitals (e.g., tetrahedral coordination of Figure 4f). For the transition elements X or Y, such as Ti, Zr, Hf, Er, and Ta, they tend to format other non-tetrahedral coordination (e.g., octahedral coordination of Figure 4e). Octahedral coordination will compete against the tetrahedral coordination of the substituted Al and is more unstable than the tetrahedral coordination of Al. Figure 4c,d shows the wave functions of the conduction band minimum of $\text{Mg}_{0.125}\text{Ti}_{0.125}\text{Al}_{0.75}\text{N}$ and $\text{Mg}_{0.125}\text{Ge}_{0.125}\text{Al}_{0.75}\text{N}$. As shown in Figure 4d, for a non-transition element, the electron cloud of the regular tetrahedron geometry to bond to the nitrogen atom does not aggregate in the c-axis. For a transition element, it might bond to the nitrogen atom along the c-axis (Figure 4c). When a strain is performed on $\text{Mg}_{0.125}\text{Ti}_{0.125}\text{Al}_{0.75}\text{N}$ with unstable coordination, atoms move away from their regular tetrahedral positions and induce a larger du , which is due to the bond along the c-axis. As a result, the non-tetrahedral coordination of transition elements X or Y is easier to increase $|du/d\epsilon|$ than the main group doping atoms with tetrahedral coordination under sp^3 hybridization. It should be noted that the atomic radius also affects the e_{33} . While the atomic radius of the doping atom is excessively large, it will produce a large local distortion in the lattice leaving a small space for an atom to move under the strain. For example, in $\text{Ba}_{0.125}\text{Ti}_{0.125}\text{Al}_{0.75}\text{N}$, the atomic radius of Ba is 2.78 \AA , and the $du/d\epsilon$ is only 0.139. In a word, a small atomic radius and d/f-electrons are two parameters for finding doped-AlN with a large e_{33} .

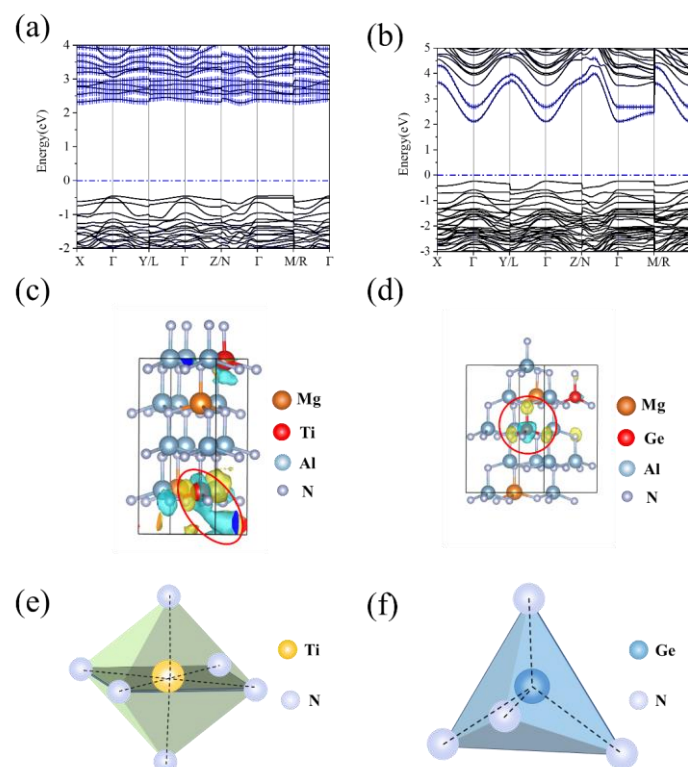


Figure 4. (a,b) Band structures of $\text{Mg}_{0.125}\text{Ti}_{0.125}\text{Al}_{0.75}\text{N}$ and $\text{Mg}_{0.125}\text{Ge}_{0.125}\text{Al}_{0.75}\text{N}$. The blue error bar respectively represents the contribution of the d-electrons of Ti and s-electrons of Ge. (c,d) Wave function analyses of $\text{Mg}_{0.125}\text{Ti}_{0.125}\text{Al}_{0.75}\text{N}$ and $\text{Mg}_{0.125}\text{Ge}_{0.125}\text{Al}_{0.75}\text{N}$ are shown in red circles. Blue represents

bonding orbitals, and yellow represents anti-bonding orbitals. (e,f) The structure of Ti_3N_4 (Octahedral coordinates) and Ge_3N_4 (Tetrahedral coordinates).

As shown in Table 2, the Q_r value of all three selected systems is higher than that of $\text{Sc}_{0.25}\text{Al}_{0.75}\text{N}$. The trends are the same for the k_{33}^2 about co-doped w-AlN material and the k_{eff}^2 about the resonator. The k_{eff}^2 and k_{33}^2 of $\text{B}_{0.125}\text{Er}_{0.125}\text{AlN}$ and $\text{Mg}_{0.125}\text{Ti}_{0.125}\text{AlN}$ are both higher than that of $\text{Sc}_{0.25}\text{Al}_{0.75}\text{N}$, except for $\text{Be}_{0.125}\text{Ce}_{0.125}\text{AlN}$, due to the high permittivity according to Equation (1).

Table 2. Resonant characteristics of the resonator based on doped/undoped w-AlN. f_s and f_p represent resonant frequency and anti-resonant frequency. k_{eff}^2 and Q_r are calculated by COMSOL software. k_{33}^2 is calculated according to Equation (1).

Piezoelectric Materials	f_s (GHz)	f_p (GHz)	Q_r (None)	k_{eff}^2 (None)	k_{33}^2 (None)
w-AlN	5.237	5.348	1603.288	0.050	0.063
$\text{B}_{0.125}\text{Er}_{0.125}\text{Al}_{0.75}\text{N}$	4.696	4.945	1420.659	0.118	0.143
$\text{Be}_{0.125}\text{Ce}_{0.125}\text{Al}_{0.75}\text{N}$	4.763	4.941	1438.494	0.086	0.100
$\text{Mg}_{0.125}\text{Ti}_{0.125}\text{Al}_{0.75}\text{N}$	4.707	5.010	1434.593	0.140	0.177
$\text{Sc}_{0.25}\text{Al}_{0.75}\text{N}$	4.632	4.846	1407.990	0.104	0.123

5. Conclusions

Based on the high-throughput workflow, more than 117 $\text{X}_{0.125}\text{Y}_{0.125}\text{Al}_{0.75}\text{N}$ compounds were examined. In addition, $\text{B}_{0.125}\text{Er}_{0.125}\text{Al}_{0.75}\text{N}$, $\text{Mg}_{0.125}\text{Ti}_{0.125}\text{Al}_{0.75}\text{N}$, and $\text{Be}_{0.125}\text{Ce}_{0.125}\text{Al}_{0.75}\text{N}$ were screened out as having a higher e_{33} , C_{33} , and d_{33} than $\text{Sc}_{0.25}\text{Al}_{0.75}\text{N}$. The Q_r of the resonators made with these three systems was higher than that of $\text{Sc}_{0.25}\text{AlN}$. The effective coupling coefficient (k_{eff}^2) of $\text{B}_{0.125}\text{Er}_{0.125}\text{AlN}$ and $\text{Mg}_{0.125}\text{Ti}_{0.125}\text{AlN}$ was also higher than that of $\text{Sc}_{0.25}\text{AlN}$, except for $\text{Be}_{0.125}\text{Ce}_{0.125}\text{AlN}$ due to the high permittivity. The C_{33} is affected by the electronegativity difference. There is a negative correlation between the ΔEd and C_{33} . The doping elements–nitrogen bond with a small ΔEd leads to a larger elastic constant C_{33} of the doped-AlN because the strength of the bond is stronger. The e_{33} is affected by the $du/d\varepsilon$ of the doping atoms. The large $du/d\varepsilon$ comes from the competition between the tetrahedra coordinates [AlN₄] of w-AlN and the non-tetrahedra coordinates of the doping elements with d-/f- electrons. This work provides a new way to find promising doped-AlN materials for 5G filters.

Supplementary Materials: The following supporting information can be downloaded at: <https://www.mdpi.com/article/10.3390/ma16051778/s1>, Figure S1: The two-dimensional sandwich structure of the resonator; Figure S2: The calculated and experimented e_{33} , C_{33} , and d_{33} of $\text{Sc}_x\text{Al}_{1-x}\text{N}$ ($x = 0\text{--}0.5$); Figure S3: (a,b) Wave function analyses of $\text{Li}_{0.125}\text{Ta}_{0.125}\text{Al}_{0.75}\text{N}$ and $\text{Li}_{0.125}\text{Sb}_{0.125}\text{Al}_{0.75}\text{N}$; Table S1: Physical parameters of the materials utilized in the simulation; Table S2: Dopants considered in this study and the result of $C_{11}\text{--}C_{12}$, $2C_{13}^2\text{--}C_{33}(C_{11} + C_{12})$, C_{66} . References [48] are cited in the supplementary materials.

Author Contributions: Conceptualization, X.Y., X.L. and W.L.; methodology, X.L.; software, X.Y., J.Z. and X.L.; validation, X.Y., X.L. and T.W.; formal analysis, X.Y. and X.L.; investigation, X.Y.; resources, W.L.; data curation, X.Y. and J.Z.; writing—original draft preparation, X.Y.; writing—review and editing, X.L., T.W. and W.L.; visualization, X.Y.; supervision, L.Z. and W.L.; project administration, L.Z., W.L. and W.Y.; funding acquisition, L.Z., W.L. and W.Y. All authors have read and agreed to the published version of the manuscript.

Funding: This research was funded by Project supported by Shanghai Technology Innovation Action Plan 2020-Integrated Circuit Technology Support Program, grant number No. 20DZ1100603.

Institutional Review Board Statement: Not applicable.

Informed Consent Statement: Not applicable.

Data Availability Statement: Not applicable

Acknowledgments: The authors would like to thank Huirong Jing at Shanghai Jiao Tong University for their discussion.

Conflicts of Interest: The authors declare no conflict of interest.

References

1. Ruby, R. A Snapshot in Time: The Future in Filters for Cell Phones. *IEEE Microw. Mag.* **2015**, *16*, 46–59. <https://doi.org/10.1109/MMM.2015.2429513>.
2. Gillenwater, T. Evolution of the Smartphone. *Microw. J.* **2017**, *60*, 40–52.
3. Hickman, A.L.; Chaudhuri, R.; Bader, S.J.; Nomoto, K.; Li, L.; Hwang, J.; Xing, H.G.; Jena, D. Next Generation Electronics on the Ultrawide-Bandgap Aluminum Nitride Platform. *Semicond. Sci. Technol.* **2021**, *36*, 044001. <https://doi.org/10.1088/1361-6641/abe5fd>.
4. Weigel, R.; Morgan, D.P.; Owens, J.M.; Ballato, A.; Lakin, K.M.; Hashimoto, K.; Ruppel, C.C.W. Microwave Acoustic Materials, Devices, and Applications. *IEEE Trans. Microw. Theory Tech.* **2002**, *50*, 738–749. <https://doi.org/10.1109/22.989958>.
5. Fu, Y.Q.; Luo, J.K.; Nguyen, N.T.; Walton, A.J.; Flewitt, A.J.; Zu, X.T.; Li, Y.; McHale, G.; Matthews, A.; Iborra, E.; et al. Advances in Piezoelectric Thin Films for Acoustic Biosensors, Acoustofluidics and Lab-on-Chip Applications. *Prog. Mater. Sci.* **2017**, *89*, 31–91. <https://doi.org/10.17863/CAM.10050>.
6. Fei, C.; Liu, X.; Zhu, B.; Li, D.; Yang, X.; Yang, Y.; Zhou, Q. AlN Piezoelectric Thin Films for Energy Harvesting and Acoustic Devices. *Nano Energy* **2018**, *51*, 146–161. <https://doi.org/10.1016/j.nanoen.2018.06.062>.
7. Qin, L.; Chen, Q.; Cheng, H.; Chen, Q.; Li, J.-F.; Wang, Q.-M. Viscosity Sensor Using ZnO and AlN Thin Film Bulk Acoustic Resonators with Tilted Polar C-Axis Orientations. *J. Appl. Phys.* **2011**, *110*, 094511. <https://doi.org/10.1063/1.3657781>.
8. Aigner, R. MEMS in RF-Filter Applications: Thin Film Bulk-Acoustic-Wave Technology. In Proceedings of the The 13th International Conference on Solid-State Sensors, Actuators and Microsystems, Seoul, Republic of Korea, 5–9 June 2005; Volume 1, pp. 5–8. Digest of Technical Papers. TRANSDUCERS '05.
9. Signore, M.A.; Rescio, G.; Pascali, C.D.; Iacovacci, V.; Francioso, L. Fabrication and Characterization of AlN-Based Flexible Piezoelectric Pressure Sensor Integrated into an Implantable Artificial Pancreas. *Sci. Rep.* **2019**, *9*, 17130. <https://doi.org/10.3390/proceedings2131037>.
10. Lefeuvre, E.; Badel, A.; Richard, C.; Petit, L.; Guyomar, D. A Comparison between Several Vibration-Powered Piezoelectric Generators for Standalone Systems. *Sens. Actuator A-Phys.* **2006**, *126*, 405–416. <https://doi.org/10.1016/j.sna.2005.10.043>.
11. Lanz, R. *Piezoelectric Thin Films for Bulk Acoustic Wave Resonator Applications: From Processing to Microwave Filters*; EPFL: Lausanne, Switzerland, 2004. <https://doi.org/10.5075/epfl-thesis-2991>.
12. Rughoobur, G. In-Liquid Bulk Acoustic Wave Resonators for Biosensing Applications, Ph.D. Thesis, University of Cambridge, Cambridge, UK, 2017.
13. Hashimoto, K. *RF Bulk Acoustic Wave Filters for Communications*; Artech House: London, UK, 2009.
14. Tasnádi, F.; Alling, B.; Höglund, C.; Wingqvist, G.; Birch, J.; Hultman, L.; Abrikosov, I.A. Origin of the Anomalous Piezoelectric Response in Wurtzite Sc_{1-x}Al_xN Alloys. *Phys. Rev. Lett.* **2010**, *104*, 137601. <https://doi.org/10.1103/PhysRevLett.104.137601>.
15. Akiyama, M.; Kamohara, T.; Kano, K.; Teshigahara, A.; Takeuchi, Y.; Kawahara, N. Enhancement of Piezoelectric Response in Scandium Aluminum Nitride Alloy Thin Films Prepared by Dual Reactive Cosputtering. *Adv. Mater.* **2009**, *21*, 593–596. <https://doi.org/10.1002/adma.200802611>.
16. Manna, S.; Talley, K.R.; Gorai, P.; Mangum, J.; Zakutayev, A.; Brennecke, G.L.; Stevanović, V.; Ciobanu, C.V. Enhanced Piezoelectric Response of AlN via CrN Alloying. *Phys. Rev. Appl.* **2018**, *9*, 034026. <https://doi.org/10.1103/PhysRevApplied.9.034026>.
17. Tholander, C.; Abrikosov, I.A.; Hultman, L.; Tasnádi, F. Volume Matching Condition to Establish the Enhanced Piezoelectricity in Ternary (Sc,Y) 0.5 (Al,Ga,In) 0.5 N Alloys. *Phys. Rev. B* **2013**, *87*, 094107. <https://doi.org/10.1103/PhysRevB.87.094107>.
18. Noor-A-alam, M.; Olszewski, O.Z.; Campanella, H.; Nolan, M. Large Piezoelectric Response and Ferroelectricity in Li and V/Nb-Ta Co-Doped w-AlN. *ACS Appl. Mater. Interfaces* **2021**, *13*, 944–954. <https://doi.org/10.1021/acsami.0c19620>.
19. Hirata, K.; Yamada, H.; Uehara, M.; Anggraini, S.A.; Akiyama, M. First-Principles Study of Piezoelectric Properties and Bonding Analysis in (Mg, X, Al)N Solid Solutions (X = Nb, Ti, Zr, Hf). *ACS Omega* **2019**, *4*, 15081–15086. <https://doi.org/10.1021/acsomega.9b01912>.
20. Manna, S.; Brennecke, G.L.; Stevanović, V.; Ciobanu, C.V. Tuning the Piezoelectric and Mechanical Properties of the AlN System via Alloying with YN and BN. *J. Appl. Phys.* **2017**, *122*, 105101. <https://doi.org/10.1063/1.4993254>.
21. Jing, H.; Wang, Y.; Wen, Q.; Cai, X.; Liu, K.; Li, W.; Zhu, L.; Li, X.; Zhu, H. Large Piezoelectric and Elastic Properties in B and Sc Co-Doped Wurtzite AlN. *J. Appl. Phys.* **2022**, *131*, 245108. <https://doi.org/10.1063/5.0090501>.
22. Uehara, M.; Shigemoto, H.; Fujio, Y.; Nagase, T.; Aida, Y.; Umeda, K.; Akiyama, M. Giant Increase in Piezoelectric Coefficient of AlN by Mg-Nb Simultaneous Addition and Multiple Chemical States of Nb. *Appl. Phys. Lett.* **2017**, *111*, 112901. <https://doi.org/10.1063/1.4990533>.
23. Yokoyama, T.; Iwazaki, Y.; Onda, Y.; Nishihara, T.; Sasajima, Y.; Ueda, M. Effect of Mg and Zr Co-Doping on Piezoelectric AlN Thin Films for Bulk Acoustic Wave Resonators. *Ferroelectr. Freq. Control.* **2014**, *61*, 1322–1328. <https://doi.org/10.1109/TUFFC.2014.3039>.

24. Van de Walle, A.; Tiwary, P.; De Jong, M.; Olmsted, D.L.; Asta, M.; Dick, A.; Shin, D.; Wang, Y.; Chen, L.Q.; Liu, Z.K. Efficient Stochastic Generation of Special Quasirandom Structures. *Calphad-Comput. Coupling Ph. Diagrams Thermochem.* **2013**, *42*, 13–18. <https://doi.org/10.1016/j.calphad.2013.06.006>.
25. John, P.; Perdew, J.P.; Kieron, Burke; Matthias; Ernzerhof; Erratum Generalized Gradient Approximation Made Simple. *Phys. Rev. Lett.* **1996**, *77*, 3865. <https://doi.org/10.1103/PhysRevLett.77.3865>.
26. Kresse, G.G.; Furthmüller, J.J. Efficient Iterative Schemes for Ab Initio Total-Energy Calculations Using a Plane-Wave Basis Set. *Phys. Rev. B* **1996**, *54*, 11169. <https://doi.org/10.1103/PhysRevB.54.11169>.
27. Kresse, G.; Joubert, D. From Ultrasoft Pseudopotentials to the Projector Augmented-Wave Method. *Phys. Rev. B* **1999**, *59*, 1758–1775. <https://doi.org/10.1103/PhysRevB.59.1758>.
28. Le Page, Y.; Saxe, P. Symmetry-General Least-Squares Extraction of Elastic Data for Strained Materials from Ab Initio Calculations of Stress. *Phys. Rev. B* **2002**, *65*, 104104. <https://doi.org/10.1103/PhysRevB.65.104104>.
29. Vanderbilt, D.; King-Smith, R.D. Electric Polarization as a Bulk Quantity and Its Relation to Surface Charge. *Phys. Rev. B* **1993**, *48*, 4442–4455. <https://doi.org/10.1103/PhysRevB.48.4442>.
30. King-Smith, R.D.; Vanderbilt, D. Theory of Polarization of Crystalline Solids. *Phys. Rev. B* **1993**, *47*, 1651–1654. <https://doi.org/10.1103/PhysRevB.47.1651>.
31. Resta, R. Macroscopic Polarization in Crystalline Dielectrics: The Geometric Phase Approach. *Rev. Mod. Phys.* **1994**, *66*, 899–915. <https://doi.org/10.1103/RevModPhys.66.899>.
32. Monkhorst, H.J.; Pack, J.D. Special Points for Brillouin-Zone Integrations. *Phys. Rev. B* **1976**, *13*, 5188–5192. <https://doi.org/10.1103/PhysRevB.13.5188>.
33. Wang, S.; Zhao, W.; Setyawati, W.; Mingo, N.; Curtarolo, S. Assessing the Thermoelectric Properties of Sintered Compounds via High-Throughput Ab-Initio Calculations. *Phys. Rev. X* **2011**, *1*, 021012. <https://doi.org/10.1103/PhysRevX.1.021012>.
34. Dudarev, S.L.; Botton, G.A.; Savrasov, S.Y.; Humphreys, C.J.; Sutton, A.P. Electron-Energy-Loss Spectra and the Structural Stability of Nickel Oxide: An LSDA+U Study. *Phys. Rev. B* **2017**, *57*, 1505–1509. <https://doi.org/10.1103/PhysRevB.57.1505>.
35. Makkonen, T.; Holappa, A.; Ella, J.; Salomea, M.M. Finite Element Simulations of Thin-Film Composite BAW Resonators. *IEEE Trans. Ultrason. Ferroelect. Freq. Contr.* **2001**, *48*, 1241–1258. <https://doi.org/10.1109/58.949733>.
36. Bi, F.Z.; Barber, B.P. Bulk Acoustic Wave RF Technology. *IEEE Microw. Mag.* **2008**, *9*, 65–80. <https://doi.org/10.1109/MMM.2008.927633>.
37. Bode, H.W. *Network Analysis and Feedback Amplifier Design*; D. Van Nostrand Company: Toronto, ON, Canada, 1945; pp. 216–221.
38. Born, M.; Huang, K.; Lax, M. Dynamical Theory of Crystal Lattices. *Am. J. Phys.* **1955**, *23*, 474. <https://doi.org/10.1119/1.1934059>.
39. Caro, M.A.; Zhang, S.; Riekkinen, T.; Ylilampi, M.; Moram, M.A.; Lopez-Acevedo, O.; Molarius, J.; Laurila, T. Piezoelectric Coefficients and Spontaneous Polarization of ScAlN. *J. Phys. Condens. Matter* **2015**, *27*, 245901. <https://doi.org/10.1088/0953-8984/27/24/245901>.
40. Zhang, Q.; Chen, M.; Liu, H.; Zhao, X.; Qin, X.; Wang, F.; Tang, Y.; Yeoh, K.H.; Chew, K.-H.; Sun, X. Deposition, Characterization, and Modeling of Scandium-Doped Aluminum Nitride Thin Film for Piezoelectric Devices. *Materials* **2021**, *14*, 6437. <https://doi.org/10.3390/ma14216437>.
41. Moreira, M.A.; Bjurström, J.; Yantchev, V.; Katardjiev, I. Synthesis and Characterization of Highly C-Textured Al(1-x)Sc(x)N Thin Films in View of Telecom Applications. *IOP Conf. Ser. Mater. Sci. Eng.* **2012**, *41*, 012014. <https://doi.org/10.1088/1757-899X/41/1/012014>.
42. Sanderson, R.T. An Interpretation of Bond Lengths and a Classification of Bonds. *Science* **1951**, *114*, 670–672. <https://doi.org/10.1126/science.114.2973.670>.
43. Li, K.; Wang, X.; Zhang, F.; Xue, D. Electronegativity Identification of Novel Superhard Materials. *Phys. Rev. Lett.* **2008**, *100*, 235504. <https://doi.org/10.1103/PhysRevLett.100.235504>.
44. Gao, F.; He, J.; Wu, E.; Liu, S.; Yu, D.; Li, D.; Zhang, S.; Tian, Y. Hardness of Covalent Crystals. *Phys. Rev. Lett.* **2003**, *91*, 015502. <https://doi.org/10.1103/PhysRevLett.91.015502>.
45. Barbe, J. Convenient Relations for the Estimation of Bond Ionicity in A-B Type Compounds. *J. Chem. Educ.* **1983**, *60*, 640. <https://doi.org/10.1021/ed060p640>.
46. Bernardini, F.; Fiorentini, V.; Vanderbilt, D. Spontaneous Polarization and Piezoelectric Constants of III–V Nitrides. *Phys. Rev. B* **1997**, *56*, 10024–10027. <https://doi.org/10.1103/PhysRevB.56.R10024>.
47. Hirata, K.; Mori, Y.; Yamada, H.; Uehara, M.; Anggraini, S.A.; Akiyama, M. Significant Enhancement of Piezoelectric Response in AlN by Yb Addition. *Materials* **2021**, *14*, 309. <https://doi.org/10.3390/ma14020309>.
48. Auld, B.A. *Acoustic Fields and Waves in Solids*; Jone Wiley & Sons: Hoboken, NJ, USA, 1973.

Disclaimer/Publisher’s Note: The statements, opinions and data contained in all publications are solely those of the individual author(s) and contributor(s) and not of MDPI and/or the editor(s). MDPI and/or the editor(s) disclaim responsibility for any injury to people or property resulting from any ideas, methods, instructions or products referred to in the content.